

Impact of numerical solution approach of a plant hydrodynamic model ([v0.1](#)) on vegetation dynamics

Yilin Fang¹, [L.](#) Ruby Leung¹, Ryan Knox², Charlie Koven², and Ben Bond-Lamberty¹

¹Pacific Northwest National Laboratory, Richland, Washington, USA

⁵2Lawrence Berkeley National Laboratory, Berkeley, California, USA

Correspondence to: Yilin Fang (yilin.fang@pnnl.gov)

Abstract. Numerous plant hydrodynamic models have started to be implemented in vegetation dynamics models, reflecting the central role of plant hydraulic traits in driving water, energy and carbon [cyclecycles](#), as well as plant adaptation to climate change. Different numerical approximations of the governing equations of the hydrodynamic models have been documented, but the numerical accuracy of these models and its subsequent effects on the simulated vegetation function and dynamics have rarely been evaluated. Using different numerical solution methods (including implicit and explicit approaches) and vertical discrete grid resolutions, we evaluated the numerical performance of a plant hydrodynamic module in the Functionally Assembled Terrestrial Ecosystem Simulator (FATES-HYDRO [version 0.1](#)) based on single point and global simulations. Our simulation results showed that when near-surface vertical grid spacing is coarsened (grid size > 10 cm), the model significantly overestimates above ground biomass (AGB) in most of the temperate forest locations, and underestimates AGB in the boreal forest locations, as compared to a simulation with finer vertical grid spacing. Grid coarsening has a small effect on AGB in the tropical zones of Asia and South America. In particular, coarse surface grid resolution should not be used when there are large and prolonged water content [difference](#)[differences](#) among soil layers at depths due to long dry season duration and/or well-drained soil, or when soil evaporation is a dominant fraction of evapotranspiration. Similarly, coarse surface grid resolution should not be used when there is lithologic discontinuity along the soil depth. This information is useful for uncertainty quantification, sensitivity analysis, or training surrogate models to design the simulations when computational cost limits the use of ensemble simulations.

30 **1 Introduction**

Vegetation plays a central role in water, energy and carbon ~~cycle~~[cycles](#) [Arora, 2002; Gerten *et al.*, 2004; Levis *et al.*, 2000] through the bidirectional interactions between climate and terrestrial biota. Stomatal conductance is one of plants' physiological properties that form the basis of evapotranspiration parameterizations in physically based hydrological models [Arora, 35 2002] and Earth system models (ESMs). Soil moisture plays a vital role in regulating stomatal conductance and plant water status [Anav *et al.*, 2018; Buckley, 2019]. How ESMs represent soil moisture regulation on stomatal conductance thus has important implications for the partitioning of evapotranspiration into evaporation and transpiration, the soil moisture profiles that influence soil hydrological processes, and plant growth and vegetation dynamics as well as the accurate 40 simulation of land-atmosphere energy and water fluxes.

Most ESMs use non-mechanistic soil moisture stress parameterizations that relate a metric of soil moisture status to attenuation of stomatal conductance in response to declining soil water under drying conditions, ignoring vegetation water use strategies [Kennedy *et al.*, 2019]. The ESM community has worked to replace such empirical water stress parameterizations with more 45 realistic mechanistic plant hydrodynamic representations. Water transport in the soil-plant-atmosphere continuum is often represented using a Richard's type equation in the mixed-form or potential-based form, which has been commonly used to describe fluid flow in partially saturated porous media [Celia *et al.*, 1990; Lehmann and Ackerer, 1998]. In the mixed-form the equation is written using both water potential and water content as the dependent variables, while the 50 equation is written using water potential as the dependent variable in potential-based form. Hydrodynamic representations are nonlinear problems, because xylem hydraulic conductivity (K_s) and plant water storage vary nonlinearly with water potential in each organ in the model, so they are typically solved numerically.

Different numerical approaches, with various degrees of simplifications, have been used in 55 the literature to solve the equations in the plant hydrodynamic models. Hydraulic models that consider water storage in the simulated plant organs may use numerical techniques that feature non-iterative (e.g., explicit time integration) or iterative approaches (e.g., Newton's method for nonlinear problems). Examples of models using non-iterative solution approach are the Soil Plant Atmosphere (SPA) model [Williams *et al.*, 1996], a dynamic water flow and storage

60 model called HydGro [Steppe *et al.*, 2006], the trait forest simulator (TFS) [Christoffersen *et al.*, 2016], ED2-hydro [Xu *et al.*, 2016], and Noah-MP-PHS [Li *et al.*, 2021]. Models that use
65 iterative solutions include FETCH2 [Mirfenderesgi *et al.*, 2016], the soil plant continuum model [Sperry *et al.*, 1998; Sperry *et al.*, 2016], and a porous media model for the hydraulic system [Chuang *et al.*, 2006]. There has however been no systematic evaluation and comparison of their
model performance and their consequential impact on evapotranspiration partitioning, soil
moisture dynamics, and vegetation function and dynamics simulated by the ESMs.

70 As key differences among different plant hydrodynamic models lie in the numerical
approaches used to solve the plant hydrodynamic equations, we implement several numerical
solution options for the hydrodynamic problems in the same model to facilitate comparison. The
75 model used here is the plant hydrodynamic model in the Functionally Assembled Terrestrial
Ecosystem Simulator (FATES-HYDRO [version 0.1](#)) for illustrations. We compare the model
performance of the various options and their impacts on simulating evapotranspiration
partitioning, soil moisture dynamics, and vegetation dynamics. Our focus is on two aspects of the
numerical solutions: vertical grid aggregation of the soil column and use of explicit vs. implicit
solvers of the hydrodynamics equations, as they have implications for the accuracy and
computational efficiency of the numerical solvers.

2 Model description

2.1 Functionally Assembled Terrestrial Ecosystem Simulator (FATES)

80 FATES is a vegetation demographic model, which uses the Ecosystem Demography (ED)
[Moorecroft *et al.*, 2001] and Perfect Plasticity Approximations (PPA) [Purves *et al.*, 2008] to
scale from cohorts of individual plants of different plant functional types growing within a
mosaic of patches with different disturbance histories to the land surface [Fisher *et al.*, 2018;
Koven *et al.*, 2020]. FATES has been coupled to the Energy Exascale Earth System Model
85 (E3SM) Land Model (ELM) [[CaldwellGolaz](#) *et al.*, 2019; Leung *et al.*, 2020], which we use
here. Processes that are simulated in FATES include physiological processes on 30 min time
steps, which include photosynthesis, respiration, and radiative transfer, as well as land-surface
energy balance and all plant-soil hydrologic calculations coordinated with the land-surface
model. At daily timescale, FATES handles plant growth, mortality, and disturbances. More

details of FATES can be found in Fisher et al. [2015] and Koven et al. [2020], as well as in the
90 online documentation https://fates-docs.readthedocs.io/en/latest/fates_tech_note.html.

The Energy Exascale Earth System Model (E3SM) is an Earth system model containing components for atmosphere, land, ocean, sea ice, and river [*Caldwell Golaz et al.*, 2019; *Leung et al.*, 2020]. The land model in E3SM, referred to as ELM, was based on the Community Land Model version 4.5 (CLM4.5) [*Oleson et al.*, 2013]. The E3SM land model for this study is
95 similar to the Community Land Model version 4.5 [*Oleson et al.*, 2013] except for some biogeochemistry components [*Ricciuto et al.* 2018; *Burrows et al.*, 2020] and a one-dimensional variably saturated subsurface flow model [*Bish et al.*, 2018], which were not turned on in this study. In ELM, the soil hydraulic properties are assumed to be a function of sand and clay contents based on the work by Clapp and Hornberger [1978] and Cosby et al. [1984], and soil
100 organic properties [Lawrence and Slater 2008]. The bulk hydraulic properties are weighted averages of the properties of the soil mineral and organic contents, and details can be found in Oleson et al. [2013]. As described in Oleson et al. [2013], the mineral soil texture dataset for each soil layer was created from the International Geosphere-Biosphere Programme (IGBP) soil dataset (Global Soil Data Task 2000) of 4931 soil mapping units and their sand and clay content
105 [Bonan et al. 2002]. The majority of the globe soil organic matter data is from ISRICWISE [Batjes, 2006], and those from the high latitudes come from the 0.25° version of the Northern Circumpolar Soil Carbon Database [*Hugelius et al.* 2012]. Both datasets report carbon down to 1m depth and carbon is partitioned across the top seven soil layers as in Lawrence and Slater [2008].

110 2.2 FATES-HYDRO

FATES-HYDRO is an extension of the plant hydrodynamic model described in Christoffersen et al. [2016]. It solves transient water flow from soil to roots, stem and leaf to meet the transpiration demand. Xylem transport in FATES-HYDRO follows Darcy's law, which says that flow rate in the porous media is proportional to the hydraulic gradient and the hydraulic
115 conductivity. FATES-HYDRO accounts for the plant internal water storage that can buffer the imbalance of root water uptake and transpiration demand. In discretized approximation, the transient water mass balance equation along the hydraulic path for each node i can be written as:

$$\rho_w V_t \frac{d\theta_t}{dt} = \sum_{j=1}^k Q_{t,j} \quad (1)$$

$$\rho_w V_i \frac{d\theta_i}{dt} = \sum_{j=1}^k Q_{i,j} \quad (1)$$

where i is the node number and i at the leaf node is equal to 1, with nodes ordered from top to bottom and horizontally from the root node to soil node (Fig.1-). Discrete fluxes between the compartment of interest and a total of k other connected compartments are indexed by j . k is 1 for the leaf node, and it is equal to 2 for compartment other than the transporting root compartment where k equals the number of soil layers plus 1. ρ_w is the density of water (kg m^{-3}), V_i is the volume of modeled compartment or node (m^3), t is time (s), θ_i is water content (dimensionless), $Q_{i,j}$ (kg s^{-1}) is the water mass flux between compartments i and j (positive for movement towards the leaf).

$$Q_{i,j} = -K_i (\rho_w g (z_i - z_j) + (\psi_i - \psi_j)) \quad (2)$$

$$Q_{i,j} = -K_i (\rho_w g (z_i - z_j) + (\psi_i - \psi_j)) \quad (2)$$

The flux over a connection is driven by potential differences between compartments, where g is acceleration due to gravity (9.81 m s^{-2}) and ψ_i is xylem or soil matric water potential (MPa), which is calculated based on pressure-volume curve, analogous to the soil water retention curve in ELM soil hydrology [Christoffersen *et al.*, 2016]; z_i is the elevation above (positive) or below (negative) the ground (m), and K_i is the conductance ($\text{kg Mpa}^{-1} \text{ s}^{-1}$) at the boundary between compartments i and j . K_i is calculated as the product of the relative hydraulic conductance $k_{r,i}$ (dimensionless) and the maximum conductance ($\text{kg mPa}^{-1} \text{ s}^{-1}$) at the boundary of nodes i . Note the maximum conductance is a product of the conduit cross-section and the material conductivity. Relative conductance or fraction of maximum conductance, $k_{r,i}$, is calculated by the vulnerability curve using an inverse polynomial function [Manzoni *et al.*, 2013] in plant compartment as follows:

$$k_{r,i} = \left[1 + \left(\frac{\psi_i}{P_{50,i}} \right)^{a_i} \right]^{-1} \quad (3)$$

$$k_{r,i} = \left[1 + \left(\frac{\psi_i}{P_{50,i}} \right)^{a_i} \right]^{-1} \quad (3)$$

P_{50} is the water potential leading to 50% loss of hydraulic conductivity, a_i is a shape index (dimensionless). The water stress function is usually empirically represented in land models as a function of soil water matric potential, but here is replaced by an empirical function of leaf water potential to include the hydraulic impacts on stomatal conductance [Christofferson *et al.* 2016]:

$$145 \quad \beta = \left[1 + \left(\frac{\psi_l}{P_{50,gs}} \right)^{a_{gs}} \right]^{-1} \quad (4)$$

$$\beta = \left[1 + \left(\frac{\psi_l}{P_{50,gs}} \right)^{a_{gs}} \right]^{-1} \quad (4)$$

where β is a water stress fraction, ψ_l is the leaf water potential (MPa), $P_{50,gs}$ is the leaf water potential ψ_l (MPa) at 50% stomatal closure, and a_{gs} is the shape parameter (dimensionless).

β modifies the top of canopy leaf photosynthetic capacity and the Ball-Berry leaf stomatal conductance as shown in Eqs. 5 and 6 below:

$$150 \quad V_{c,max} = \beta V_{c,max} \quad (5)$$

$$g_s = m \frac{A_n}{C_s/P_{atm}} h_s + \beta b \quad (6)$$

where $V_{c,max}$ is the maximum rate of carboxylation ($\mu\text{mol CO}_2 \text{ m}^{-2} \text{ s}^{-1}$), g_s is the leaf stomatal conductance ($\mu\text{mol m}^{-2} \text{ s}^{-1}$), m is a plant functional type dependent parameter, A_n is leaf net photosynthesis ($\mu\text{mol CO}_2 \text{ m}^{-2} \text{ s}^{-1}$), C_s is the leaf surface CO_2 partial pressure (Pa), P_{atm} is the atmospheric pressure (Pa), h_s is the leaf surface humidity, and b is the minimum stomatal conductance ($\mu\text{mol m}^{-2} \text{ s}^{-1}$), β is the stress factor defined by Eq. 4.

Hydraulic failure induced mortality will be triggered when the plant fractional loss of conductivity (f_{tc}) reaches a threshold ($f_{tc,t}$, default is 0.5):

$$M_{hf,coh} = \begin{cases} \frac{f_{tc} - f_{tc,t}}{1 - f_{tc,t}} m_{ft} & \text{for } f_{tc} \geq f_{tc,t} \\ 0.0 & \text{for } f_{tc} < f_{tc,t} \end{cases} \quad (7)$$

160 where m_{ft} is the maximum mortality rate (yr^{-1}), f_{tc} is the maximum of $(1 - k_{r,i})$ for i in plant compartments, $k_{r,i}$ is defined in Eq. 3.

165 FATES-HYDRO divides each individual tree into four compartments: leaf, stem, transporting root (troot), and absorbing root (aroot) as shown in Figure 1. In this study, all compartments except for the absorbing root are represented by a single node for each in the discrete approximation of the equation. The absorbing root is discretized into the same number of nodes as the number of soil layers for soil hydrology in ELM. The soil in each layer is 170 radially discretized into cylindrical shells representing the rhizosphere around an absorbing root (Fig. 1). [An example discretization with explicit compartment numbers is shown in Figure S1 in the Supplement and Eq. 1 for each compartment are listed in the Supplement as well to demonstrate how each compartment interacts with the others, including the soil-root interaction.](#)

2.3 Numerical solutions

175 We provide the following options to solve Equation 1, including non-iterative and iterative approaches. For the non-iterative approach, as the time step in FATES for fast processes is 30 min, we use a sub-stepping time integration, with a sub-time step of 10 min, following the timestep used in ED2 [Xu *et al.*, 2016]. Nonlinear iterative methods, including the Newton and Picard schemes, are commonly used to solve Richards' equation [Albuja and Avila, 2021; Brenner and Cances, 2017; Caviedes-Voullieme *et al.*, 2013; Celia *et al.*, 1990; Lehmann and Ackerer, 1998; List and Radu, 2016]. The Picard scheme is a globally convergent method with a low solution efficiency because of its first-order convergence rate. On the other hand, the 180 Newton method is only locally convergent, but a converged solution is not always guaranteed. In this study, we use the Newton method.

We use water content θ in each compartment as unknowns for the Newton iteration. Coupled with a backward Euler approximation in time, the residual form of Eq. 1 for each compartment is defined as

185

$$Re_i = \rho_w V_i \frac{\theta_i^{n+1,m+1} - \theta_i^n}{\Delta t} - \sum_{j=1}^k Q_{i,j}^{n+1,m+1} \quad (5)$$

$$Re_i = \rho_w V_i \frac{\theta_i^{n+1,m+1} - \theta_i^n}{\Delta t} - \sum_{j=1}^k Q_{i,j}^{n+1,m+1} \quad (8)$$

Superscripts n and m denote time level and iteration number, Re_i is the residual for compartment i . The correction quantity δ of water content θ at each point from the last iteration is written as

$$\delta^m = \theta^{n+1,m+1} - \theta^{n+1,m} \quad (6)$$

δ

$$\delta^m = \theta^{n+1,m+1} - \theta^{n+1,m} \quad (9)$$

190

δ^m is the solution of the following matrix equation

$$[A]\{\delta\} = -[Re] \quad (7)$$

$$[A]\{\delta\} = -[Re] \quad (10)$$

where A is the Jacobian matrix calculated from the derivative of the non-linear function in Eq. 58 with respect to the unknown water content at each point compartment, and each row in Eq. 7 is

$$(A\delta)_i = \sum_{j=1}^k C_j \delta_j; C_j = \frac{\partial Re_i}{\partial \theta_j^{n+1,m}}. \quad 10 \text{ is}$$

$$(A\delta)_i = \sum_{j=1}^k C_j \delta_j \quad (11)$$

$$C_j = \frac{\partial Re_i}{\partial \theta_j^{n+1,m}} \quad (12)$$

195

Taking compartment i connected to compartments $i-1$ and $i+1$ as an example, and expanding the water flux $Q^{n+1,m+1}$ in a truncated Taylor series with respect to water content θ at the expansion point $\theta^{n+1,m+1}$, i.e., $\theta^{n+1,m}$, we obtain

$$Q^{n+1,m+1} = Q^{n+1,m} + \frac{dQ}{d\theta} \Big|_{n+1,m} (\theta^{n+1,m+1} - \theta^{n+1,m}) + O(\delta^2) \quad (8)$$

$$Q^{n+1,m+1} = Q^{n+1,m} + \frac{dQ}{d\theta} \Big|_{n+1,m} (\theta^{n+1,m+1} - \theta^{n+1,m}) + O(\delta^2) \quad (13)$$

200

Neglecting the higher order terms, the i^{th} row in Eq. 710 becomes

$$\frac{\frac{\partial Q_{i-1}^{n+1,m}}{\partial \theta_{i-1}^{n+1,m}} \delta_{i-1}^m + \frac{\rho_w V_t}{\Delta t} \delta_t^m + \frac{\partial Q_i^{n+1,m}}{\partial \theta_i^{n+1,m}} \delta_i^m - \frac{\partial Q_i^{n+1,m}}{\partial \theta_{i+1}^{n+1,m}} \delta_{i+1}^m}{\rho_w V_t \frac{\theta_i^{n+1,m} - \theta_i^n}{\Delta t}} = Q_t^{n+1,m} - Q_{i-1}^{n+1,m} \quad (9)$$

205

$$\begin{aligned} & \frac{\partial Q_{i-1}^{n+1,m}}{\partial \theta_{i-1}^{n+1,m}} \delta_{i-1}^m + \frac{\rho_w V_i}{\Delta t} \delta_i^m + \frac{\partial Q_{i-1}^{n+1,m}}{\partial \theta_i^{n+1,m}} \delta_i^m - \frac{\partial Q_i^{n+1,m}}{\partial \theta_i^{n+1,m}} \delta_i^m - \frac{\partial Q_i^{n+1,m}}{\partial \theta_{i+1}^{n+1,m}} \delta_{i+1}^m \\ &= Q_i^{n+1,m} - Q_{i-1}^{n+1,m} - \rho_w V_i \frac{\theta_i^{n+1,m} - \theta_i^n}{\Delta t} \end{aligned} \quad (14)$$

Equation 710 is solved during each iteration. Convergence of the Newton iteration is achieved when the maximum residual is less than 10^{-8} or when the following inequality is satisfied at all nodes i :

$$\delta_t^m < \tau \quad (10)$$

$$\delta_i^m < \tau \quad (15)$$

210

where τ is the specified tolerance/accuracy. If the scheme is not convergent within the specified maximum number of iterations during a time step, Eq. 1 is explicitly integrated using sub-time stepping within each time step such that the Courant-Friedrichs-Lowy condition [Courant *et al.*, 1928] is below 1.0.

215

The stack of vertical soil-root interaction layers can be customized by the user to save computation time or carry out a grid convergence study, where a series of grids are generated and model computations are performed to analyze the differences among the results with each grid configuration. In our model configuration, the top soil layer thickness can be as thin as a few centimeters.

220

Boundary conditions for the system include transpiration flux through leaves and zero-flux for the outermost rhizosphere element assuming the rhizosphere shells encompass the whole soil layer. The rate of water mass change in each soil layer during a time step of FATES-HYDRO is passed to the land model as a source/sink term to calculate the soil water state for the next time

step. This rate differs from the transpiration sink as water can be stored or lost in the
225 compartments.

2.4 Grid aggregation

In the default model setting, there are a total of 10 soil layers. Soil layers are the discrete
vertical interval over which ELM resolves water content. ELM updates water content via
230 processes of vertical percolation, infiltration, evaporation, and through runoff and drainage of
uppermost and lowermost layers respectively. The water content in each of these layers is
presented as an initial condition to FATES-HYDRO. The grid thickness varies from 1.7 cm at
the top layer to 1.5 m at the bottom layer. The thickness for layers 2, 3, 4, 5 is 2.76 cm, 4.55 cm,
7.5 cm, and 12.3 cm, respectively. To reduce computation time and avoid potential numerical
235 stability issues caused by the thin layers, the FATES-HYDRO model can be configured such that
several soil layers are aggregated to solve for a fewer number of equations. We define a
“rhizosphere layer” as a discrete vertical interval that may contain one or more discrete soil
layers, over which the water contents and the fluxes in fine-root tissues are resolved. For
simplicity, the depth of the first rhizosphere layer for FATES-HYDRO aligns with the depth of
240 the last soil layer that’s been aggregated, and the rest of the rhizosphere layer thickness is the
same as those from ELM at the same depth. For example, as shown in Figure 2, if the first 4 soil
layers (s1 to s4) in ELM are aggregated to form the first rhizosphere layer r1 in FATES-
HYDRO, the thickness of r1 is the sum of the thickness of s1 to s4, and the thickness of r2 is the
245 same as s5, and so on. Total water mass in s1 to s4 are assigned to r1. After FATES-HYDRO is
solved, the flux exchange between the root and the rhizosphere for r1 is proportionally assigned
to s1, s2, s3, and s4 weighted by the product of soil layer thickness and hydraulic conductivity of
s1 to s4.

3 Simulation Experiments

250 Global and point-scale simulations were performed to assess the impact of vertical soil layer
aggregation. A 4×5 degree resolution global simulation was run for 100 years with two
rhizosphere grid configurations: 1) no soil layer aggregation, i.e., rhizosphere soil layers in

255 FATES-HYDRO are the same as ELM soil layers, [referred to as Reference case](#); and 2) aggregating the top 5 ELM soil layers, [referred to as Experiment case](#). A repeating cycle of a three-year (2000-2002) atmospheric forcing data from Qian et al. [2006] is used to drive the model.

260 Four locations were selected after analyzing the global simulation to further evaluate model performances using different approaches. For point-scale at selected locations, simulations with aggregation of 1, 3, 5 and 7 layers were first run using the implicit approach to check for model differences in AGB. If large differences were found between simulations, extra simulations of different layer aggregations for some points were run to determine which scheme starts to cause large difference and the relative computation costs. Each point was also simulated using the explicit approach for comparison with the implicit approach.

265 **3.1 Global simulation**

270 It takes longer time to solve more equations. The wall clock time for the simulation using no aggregation ([Reference case](#)) is 1.5 times of that for the simulation using 5-layer aggregation- ([Experiment case](#)). The difference in above ground biomass (AGB) using different layer aggregation strategies varies by regions, regardless of the total number of simulation years (Fig. 3). It took about 20 days using 120 processor cores to complete 100-year simulation for the simulation without layer aggregation. Model differences with and without soil layer aggregations were evident during a much earlier simulation year, for example year 15.

275 We found that when more rhizosphere soil layers near the surface are aggregated, the [model](#)[Experiment case simulates](#) significantly [overestimates](#)[more](#) AGB ([negative](#)[positive](#) Δ AGB in Fig 3b[3a](#)) in most of the temperate forest locations and [underestimates](#)[less](#) AGB in the boreal forest locations relative to [the](#)[Reference](#) simulation [in which soil layers are not aggregated](#). Layer aggregation has only small effects on AGB (< 5%) in tropical zones near Asia and South America. Δ AGB follows the same pattern as the differences in ET (Δ ET) (Fig. 3e[3b](#)). In general, regions with large Δ AGB have small AGB. In the southern hemisphere where Δ AGB is high, the annual mean of soil water saturation in the soil layer at the ground surface is generally lower than that in the soil layer 17 cm (layer 5) below the surface (negative soil water saturation

1 differences between soil layer 1 and layer 5 (ΔS_{l15}) in Fig. 3d3c) and the opposite (positive
2 ΔS_{l15}) is true in a large fraction of the northern hemisphere. That is, mixing of soil water from
3 layers of contrasting water saturation when aggregating grids is the main cause of ΔAGB . Using
4 285 diameter growth increment (DDBH) to represent growth, we compared the difference between
5 the absolute percentage increase of growth and absolute percentage increase of mortality caused
6 by model differences and found mixed influence of growth and mortality on AGB due to soil
7 moisture (Fig. 3d), and there are no specific patterns. However, most of the land pixels show soil
8 moisture has larger impact on growth than mortality. Compared to the percent change of AGB,
9 290 the Experiment case has larger effect on ET (Fig. 3e) in the northern hemisphere, but overall
10 small effect on water use efficiency (WUE) (Fig. 3f), which is defined as the ratio of gross
11 primary productivity (GPP) and ET.

12 Negative soil water saturation differences ΔS_{l15} between the shallow and deep soil layers can
13 be caused by long dry season durations and/or when the soil is well-drained (rapid decrease of
14 295 water content with matric potential in the capillary region); regions with large ΔAGB exhibit low
15 clay content and/or long duration of dry seasons (Fig. 4). The dry season duration is calculated as
16 the number of months when evapotranspiration is larger than precipitation. For example, ΔAGB
17 is big in the temperate forest regions which exhibit large organic matter density compared to the
18 deeper soil layers (Fig. 4f), but the soils in those regions mostly have low and relatively
19 300 homogeneous clay content (Fig 4c,e). ΔAGB in Amazon is small because of the high clay
20 content (> 30%) and short dry season durations.

21 In the high latitudes, layer aggregation schemes can still cause large difference in AGB even
22 in places with high clay content and short dry season duration because frozen soil can cause large
23 water content differences in surface soil layers. Ice in the soil can greatly decrease the hydraulic
24 305 conductivity of the soil through a power law form of the ice-impedance factor, leading to nearly
25 impermeable soil layers [Swenson *et al.*, 2012]. A large fraction of the high latitudes has high
26 ratios of soil evaporation to evapotranspiration ratio (E/ET) (Fig. 4b). E is determined by the
27 near surface soil water states, and a large ratio of E/ET can cause significant water content
28 difference in soil layers. Therefore, the simulated AGB will be significantly changed if the
29 310 surface soil is aggregated with the deeper wetter soil. Note that this simulation is not calibrated,
30 thus the high E/ET ratio at the high latitudes may be overestimated.

3.2 Interpretation of the model difference by machine learning

To confirm the factors such as E/ET ratio and soil property discontinuity along depth are the driving factors for the model differences when aggregating grids in the global simulations, we calculated ΔAGB between the results from the simulation using no layer aggregation and the 5-layer aggregation, averaged from the last five years of the simulation, and classified the grids with difference greater than 5% as “Positive Difference” (i.e., more AGB from ~~no grid aggregation~~ the Experiment case), less than ~~-5%~~ as “Negative Difference” (i.e., more AGB from the Reference case), and the rest as “Comparable”. We then constructed a machine learning model to evaluate the classification skills using the XGBoost classifier from the scikit-learn package in Python and model explanation using SHapley Additive exPlanations (SHAP) by providing impact of features on individual predictions [Lundberg and Lee, 2017]. We developed a model using the following inputs including environmental variables: surface elevation, clay content in soil layers 1 to 5 (clay_11, clay_12, clay_13, clay_14, and clay_15), clay content difference between the top 1 and the average of the top 5 layers (dc1c5), organic matter (OM) density in soil layers 1 to 5 (org_11, org_12, org_13, org_14, and org_15) and the OM density difference between the top 1 and the average of the top 5 layers (do1o5), precipitation, and temperature, and model dependent variables: soil evaporation-to-evapotranspiration ratio (efrac), dry season duration (mon_dry), soil water ~~saturation potential~~ from the top five soil layers near the ground surface (sw1, sw2, sw3, sw4, sw5). Clay content and organic matter density were selected as features because they determine hydraulic conductivity. Model dependent variables were selected to understand the physical process drivers of modeled AGB discrepancy. The machine learning classifier accuracy for the training and test data set are ~~87.85%~~ and ~~67.75%~~, respectively (Figure 5). ~~Though not so good according to a general rule~~ There is 37% improvement over the theoretical baseline of ~~thumb, random guessing, and~~ both training and test data exhibit consistent feature importance.

SHAP feature importance confirmed some of our previous hypothesis explaining the model differences. ~~Dry season duration (feature mon_dry) has relatively small importance in explaining the negative model difference.~~ The top 5 SHAP values for positive model differences in AGB include dc1c5, do1o5, mon_dry, and org_12, while those responsible for negative model differences in AGB are dc1c5, do1o5, preep, sw5, and sw2, while those responsible for positive model differences are dc1e5, sw4, preep, temp, org_13, org_14, and org_15. Temperature

becomes important because it affects the presence of soil ice in high latitudes, which affects soil
345 hydraulic conductivity. Features [efraesw3](#), [sw4](#), [dc1c5](#), [preep](#), [org_11](#), and elev are important
explaining small model differences in AGB. Because of the dependencies of efrac and mon_dry
on soil moisture and soil hydraulic conductivity (affected by soil texture and ice), it is not
surprising that soil water [saturation](#) in deep soil layer is important explaining the model
350 differences. The deep soil water status can affect soil wetness in the rhizosphere soil shell when
there is large contrast between the soil water [content](#)[potential](#) simulated by ELM between the top
and deep soil layers.

3.3 Single point simulations

To further understand the effect of soil layer aggregation, we selected a point in the tropical
355 zone (P1, (10° N, 80° W)), temperate zone (P2, (46° N, 95° W)), polar zone (P3, (66° N, 15° E)),
and equatorial zone (P4, (6° S, 135° E)), respectively from the global simulation and ran a one-
hundred year simulation subjecting to a repeating cycle of a three-year (2000-2002) atmospheric
360 forcing from Qian et al. [2006] at each selected location (Fig. [S1S2](#)). Default FATES-HYDRO
parameters are used without modification. Different rhizosphere grid configurations and
numerical schemes were run and compared for each point. The clay content and organic matter
density at each point are listed in Table S1. At P1 to P3 the clay content is around 30%, 36%,
and 21%, respectively, and it varies from 35% to 26% from the top to the bottom of soil at P4.
Organic matter density varies the most with depth at P3.

365 3.3.1 Aggregation schemes

At the end of the simulation, the fraction of wall clock time of simulations at each point using
3, 5, and 7 layer aggregations are around 0.8, 0.7, and 0.5 times of the that from the simulation
with no layer aggregation.

AGB at point P1 starts to show significant difference (49.3% on average compared to no
370 aggregation) when only two rhizosphere layers are simulated, i.e., aggregating the top 9 layers
for the surface soil (Fig. 6). For P2, aggregating 5 layers and more can result in more than 12%
of AGB difference compared to no aggregation. The same is true for points P3 and P4, with
larger differences for more layer aggregation. This kind of AGB difference between different

layer aggregation schemes show up early in the simulation as shown in Figure 7 for the 10-year simulation comparison. This means one does not need to run the full simulation to test whether layer aggregation will cause large AGB errors if computation cost is a concern. [We found at these four sites, ET \(Fig. S3\) and WUE \(Fig. S4\) are not as significantly affected by layer aggregations as AGB.](#)

At P1, the largest difference in water content is in February, the driest month, while the difference is trivial in the other months (Fig. 8). Because the dry season duration is short, and clay content is relatively homogeneous at P1, aggregating the surface layers at this point does not cause large difference in AGB. Layers 4 and deeper at P2 and P3 are affected by ice impedance, creating large difference from the top 3 layers. The water content at P3 is also affected by the large contrast in organic matter density between the surface layer and deeper soil from layer 4. At P4, lithologic discontinuity (clay content separation) between the top 3 layers and bottom layers can cause inaccuracy in soil water content, hence AGB.

[Note that the response of AGB to the number of soil layers aggregated is nonlinear because of the nonlinearity of soil water retention curve and plant vulnerability curve and different layer soil properties, which will consequentially affect when growth or mortality will be more affected by the changing soil water status.](#)

3.3.2 Integration Methods

Implicit and explicit integrations of Eq. 1 for points P1 to P4 were run to evaluate model performance and computation costs. The simulations were performed without layer aggregation for comparison of the integration schemes. The time step for the explicit integration is 10 min. There are discrepancies between the two integration approaches at P1, but results show less than 2% AGB difference at the end of the simulation year (Fig. 9). Results at P2 to P4 are almost identical. However, simulations took more time using the explicit integration approach, with wall clock times 1.85, 1.31, 1.93, and 1.72 times of that of the implicit integration for P1 to P4, respectively.

[Note that FATES is part of an earth system model, which is expected to predict plant-soil hydraulic fluxes in innumerable conditions and extremes, over potentially long periods of time.](#)

The explicit approach is easier to implement than the implicit approach in terms of coding.

405 However, the explicit approach tends to have stability issue and requires small time steps, while the implicit approach is stable using large time steps but may require many iterations to converge to a solution. ~~These numerical experiments with different integration schemes here~~ We acknowledge there are other solvers that have been used effectively in hydraulic simulations (e.g., Crank-Nicholson, etc.), but there is often no best solver. The hydraulic solvers in this study 410 were chosen based on the need to prioritize numerical stability for long simulations, which de-emphasizes the use of explicit solvers. The numerical experiments with different integration schemes in this study can serve as benchmark against each other. In the meantime, it shows that the 10-min time step in ED2 [Xu *et al.*, 2016] is a reasonable time step for these single point tests, but it is always a good practice to do convergence and stability tests for a specific study.

415 As a matter of fact, our one-year global simulation for the Reference case using the explicit integration and 10- min time step can result in more than 10% of AGB difference compared to the implicit approach.

4 Conclusions

We have implemented multiple numerical schemes in solving plant hydrodynamic equations, 420 including explicit and implicit iterative integration of Eq. 1, as well as aggregating rhizosphere soil layers for the considerations of computation cost and numerical difficulties. While not exhaustive, our results showed that explicit integration using a 10-min time step results in comparable AGB with the implicit method, but takes longer simulation time. We also found that care should be taken when configuring soil layering as it can significantly affect AGB results.

425 Large water content differences among soil layers at depth can occur due to lithologic discontinuity, long dry season duration, high E/ET ratio, or well-drained soil. Short time simulation tests can be sufficient to evaluate how model configurations or numerical approaches will affect the simulated AGB accuracy. The cost and accuracy using alternative grid aggregation methods (e.g., fewer number of cylindrical shells), and the approach to pass flux from aggregated 430 layers back to ELM soil layers can be further investigated in the future. The results from our analysis are useful for uncertainty quantification, sensitivity analysis, or training surrogate models to design the simulations when computation cost is limiting the selection of ensemble simulations.

435 *Code Availability.* The FATES-HYDRO code is available at
<https://doi.org/10.5281/zenodo.6461878>.

Author contributions. YF, RK, CK developed the code. YF set up the model, performed simulations and prepared the figures. YF, LRL, RK, CK, BB contributed to writing and editing.

Competing interests. The authors declare that they have no conflict of interest.

440 **Acknowledgements**

This research was supported by the U.S. Department of Energy Office of Science Biological and Environmental Research through the Earth System Development program as part of the Energy Exascale Earth System Model (E3SM) project. The Pacific Northwest National Laboratory (PNNL) is operated for DOE by Battelle Memorial Institute under contract DE-AC05-

445 76RLO1830.

References

Albuja, G., and A. I. Avila (2021), A family of new globally convergent linearization schemes for solving Richards' equation, *Appl Numer Math*, 159, 281-296, doi:10.1016/j.apnum.2020.09.012.

Anav, A., C. Proietti, L. Menut, S. Carnicelli, A. De Marco, and E. Paoletti (2018), Sensitivity of stomatal conductance to soil moisture: implications for tropospheric ozone, *Atmos Chem Phys*, 18(8), 5747-5763, doi:10.5194/acp-18-5747-2018.

Arora, V. (2002), Modeling vegetation as a dynamic component in soil-vegetation-atmosphere transfer schemes and hydrological models, *Rev Geophys*, 40(2), doi:Artn 1006 10.1029/2001rg000103.

Batjes, N.H., 2006. ISRIC-WISE derived soil properties on a 5 by 5 arc-minutes global grid. Report 2006/02 (available through : <http://www.isric.org>)

Bisht, G., W. J. Riley, G. E. Hammond, and D. M. Lorenzetti (2018), Development and evaluation of a variably saturated flow model in the global E3SM Land Model (ELM) version 1.0, *Geosci Model Dev*, 11(10), 4085-4102, doi:10.5194/gmd-11-4085-2018.

Bonan, G.B., S. Levis, L. Kergoat, and K. W. Oleson (2002). Landscapes as patches of plant functional types: An integrating concept for climate and ecosystem models. *Global Biogeochem. Cycles* 16: 5.1-5.23.

Brenner, K., and C. Cances (2017), Improving Newton's Method Performance by Parametrization: The Case of the Richards Equation, *Siam J Numer Anal*, 55(4), 1760-1785, doi:10.1137/16m1083414.

Buckley, T. N. (2019), How do stomata respond to water status?, *New Phytol*, 224(1), 21-36, doi:10.1111/nph.15899.

Buotte, P. C., et al. (2021), Capturing functional strategies and compositional dynamics in vegetation demographic models, *Biogeosciences*, 18(14), 4473-4490, doi:10.5194/bg-18-4473-2021.

475 Burrows, S. M., et al. (2020), The DOE E3SM v1.1 Biogeochemistry Configuration: Description and Simulated Ecosystem-Climate Responses to Historical Changes in Forcing, *J Adv Model Earth Sy*, 12(9), doi:ARTN e2019MS001766

~~Caldwell, P. M(2019), The DOE E3SM Coupled Model Version 1: Description and Results at High Resolution, *J Adv Model Earth Sy*, 11(12), 4095-4146, doi:10.1029/2019ms001870.~~

480 Caviedes-Voullieme, D., P. Garcia-Navarro, and J. Murillo (2013), Verification, conservation, stability and efficiency of a finite volume method for the 1D Richards equation, *J Hydrol*, 480, 69-84, doi:10.1016/j.jhydrol.2012.12.008.

485 Celia, M. A., E. T. Bouloutas, and R. L. Zarba (1990), A General Mass-Conservative Numerical-Solution for the Unsaturated Flow Equation, *Water Resour Res*, 26(7), 1483-1496, doi:Doi 10.1029/90wr00196.

Christoffersen, B. O., et al. (2016), Linking hydraulic traits to tropical forest function in a size-structured and trait-driven model (TFS v.1-Hydro), *Geosci Model Dev*, 9(11), 4227-4255, doi:10.5194/gmd-9-4227-2016.

490 Clapp, R. B., and G. M. Hornberger (1978), Empirical Equations for Some Soil Hydraulic-Properties, *Water Resour Res*, 14(4), 601-604, doi:10.1029/Wr014i004p00601.

Cosby, B.J., Hornberger, G.M., Clapp, R.B., and Ginn, T.R. 1984. A statistical exploration of the relationships of soil moisture characteristics to the physical properties of soils. *Water Resour. Res.* 20:682-690.

495 Chuang, Y. L., R. Oren, A. L. Bertozi, N. Phillips, and G. G. Katul (2006), The porous media model for the hydraulic system of a conifer tree: Linking sap flux data to transpiration rate, *Ecol Model*, 191(3-4), 447-468, doi:10.1016/j.ecolmodel.2005.03.027.

Fisher, R. A., et al. (2018), Vegetation demographics in Earth System Models: A review of progress and priorities, *Global Change Biol*, 24(1), 35-54, doi:10.1111/gcb.13910.

500 Fisher, R. A., et al. (2015), Taking off the training wheels: the properties of a dynamic vegetation model without climate envelopes, CLM4.5(ED), *Geosci Model Dev*, 8(11), 3593-3619, doi:10.5194/gmd-8-3593-2015.

Gerten, D., S. Schaphoff, U. Haberlandt, W. Lucht, and S. Sitch (2004), Terrestrial vegetation and water balance - hydrological evaluation of a dynamic global vegetation model, *J Hydrol*, 286(1-4), 249-270, doi:10.1016/j.jhydrol.2003.09.029.

505 Global Soil Data Task 2000. Global soil data products CD-ROM (IGBP-DIS). International Geosphere-Biosphere Programme-Data and Information Available Services [Available online at <http://www.daac.ornl.gov>].

[Golaz, J. C. et al. \(2019\), The DOE E3SM Coupled Model Version 1: Overview and Evaluation at Standard Resolution, *J Adv Model Earth Sy*, 11\(7\), 2089-2129, doi:10.1029/2018ms001603.](#)

510 Hugelius, G., C. Tarnocai, G. Broll, J.G. Canadell, P. Kuhry, adn D.K. Swanson, 2012. The Northern Circumpolar Soil Carbon Database: spatially distributed datasets of soil coverage and soil carbon storage in the northern permafrost regions. *Earth Syst. Sci. Data Discuss.*, 5, 707-733 (available online at (<http://dev1.geo.su.se/bbcc/dev/ncscd/>).

515 Kennedy, D., S. Swenson, K. W. Oleson, D. M. Lawrence, R. Fisher, A. C. L. da Costa, and P. Gentine (2019), Implementing Plant Hydraulics in the Community Land Model, Version 5, *J Adv Model Earth Sy*, 11(2), 485-513, doi:10.1029/2018ms001500.

520 Koven, C. D., et al. (2020), Benchmarking and parameter sensitivity of physiological and vegetation dynamics using the Functionally Assembled Terrestrial Ecosystem Simulator (FATES) at Barro Colorado Island, Panama, *Biogeosciences*, 17(11), 3017-3044, doi:10.5194/bg-17-3017-2020.

Lawrence, D.M., and Slater, A.G. (2008). Incorporating organic soil into a global climate model. *Clim. Dyn.* 30. DOI:10.1007/s00382-007-0278-1.

525 Lawrence, D. M., et al. (2019), The Community Land Model Version 5: Description of New Features, Benchmarking, and Impact of Forcing Uncertainty, *J Adv Model Earth Sy*, 11(12), 4245-4287, doi:10.1029/2018ms001583.

Lehmann, F., and P. H. Ackerer (1998), Comparison of iterative methods for improved solutions of the fluid flow equation in partially saturated porous media, *Transport Porous Med*, 31(3), 275-292, doi:Doi 10.1023/A:1006555107450.

530 Leung, L. R., D. C. Bader, M. A. Taylor, and R. B. McCoy (2020), An Introduction to the E3SM Special Collection: Goals, Science Drivers, Development, and Analysis, *J Adv Model Earth Sy*, 12(11), doi:ARTN e2019MS001821 10.1029/2019MS001821.

Levis, S., J. A. Foley, and D. Pollard (2000), Large-scale vegetation feedbacks on a doubled CO₂ climate, *J Climate*, 13(7), 1313-1325, doi:Doi 10.1175/1520-0442(2000)013<1313:Lsvfoa>2.0.Co;2.

535 Li, L. C., Z. L. Yang, A. M. Matheny, H. Zheng, S. C. Swenson, D. M. Lawrence, M. Barlage, B. Y. Yan, N. G. McDowell, and L. R. Leung (2021), Representation of Plant Hydraulics in the Noah-MP Land Surface Model: Model Development and Multiscale Evaluation, *J Adv Model Earth Sy*, 13(4), doi:ARTN e2020MS002214 10.1029/2020MS002214.

540 List, F., and F. A. Radu (2016), A study on iterative methods for solving Richards' equation, *Computat Geosci*, 20(2), 341-353, doi:10.1007/s10596-016-9566-3.

Lundberg, S. M., and S. I. Lee (2017), A Unified Approach to Interpreting Model Predictions, *Adv Neur In*, 30.

545 Manzoni, S., Vico, G., Katul, G., Palmroth, S., Jackson, R. B., and Porporato (2013), A.: Hydraulic limits on maximum plant transpiration and the emergence of the safety-efficiency trade-off, *New Phy- tol.*, 198, 169–178, doi: 10.1111/nph.12126

Mirfenderesgi, G., G. Bohrer, A. M. Matheny, S. Fatichi, R. P. D. Frasson, and K. V. R. Schafer (2016), Tree level hydrodynamic approach for resolving aboveground water storage and stomatal conductance and modeling the effects of tree hydraulic strategy, *J Geophys Res Biogeo*, 121(7), 1792-1813, doi:10.1002/2016jg003467.

550 Moorcroft, P. R., G. C. Hurtt, and S. W. Pacala (2001), A method for scaling vegetation dynamics: The ecosystem demography model (ED), *Ecol Monogr*, 71(4), 557-585, doi:10.1890/0012-9615(2001)071[0557:Amfsvd]2.0.Co;2.

Oleson, K. W., et al. (2013), Technical description of version 4.5 of the Community Land Model (CLM), NCAR Tech. Note, NCAR/TN-503+STR, Research, Boulder, Colorado, National Center for Atmospheric. *Rep.*, 420 pp, .

555 Purves, D. W., Lichstein, J. W., Strigul, N., and Pacala, S. W. (2008) Predicting and understanding forest dynamics using a simple tractable model, *P Natl Acad Sci USA* 105, 17018-17022.

560 Qian, T. T., A. Dai, K. E. Trenberth, and K. W. Oleson (2006), Simulation of global land surface conditions from 1948 to 2004. Part I: Forcing data and evaluations, *J Hydrometeorol*, 7(5), 953-975, doi:Doi 10.1175/Jhm540.1.

565 Ricciuto, D., K. Sargsyan, and P. Thornton (2018), The Impact of Parametric Uncertainties on
Biogeochemistry in the E3SM Land Model, *J Adv Model Earth Sy*, 10(2), 297-319,
doi:10.1002/2017ms000962.

Sperry, J. S., F. R. Adler, G. S. Campbell, and J. P. Comstock (1998), Limitation of plant water
use by rhizosphere and xylem conductance: results from a model, *Plant Cell Environ*,
21(4), 347-359, doi:DOI 10.1046/j.1365-3040.1998.00287.x.

570 Sperry, J. S., Y. J. Wang, B. T. Wolfe, D. S. Mackay, W. R. L. Anderegg, N. G. McDowell, and
W. T. Pockman (2016), Pragmatic hydraulic theory predicts stomatal responses to
climatic water deficits, *New Phytol*, 212(3), 577-589, doi:10.1111/nph.14059.

Steppe, K., D. J. W. De Pauw, R. Lemeur, and P. A. Vanrolleghem (2006), A mathematical
model linking tree sap flow dynamics to daily stem diameter fluctuations and radial stem
growth, *Tree Physiol*, 26(3), 257-273, doi:DOI 10.1093/treephys/26.3.257.

575 Swenson, S. C., D. M. Lawrence, and H. Lee (2012), Improved simulation of the terrestrial
hydrological cycle in permafrost regions by the Community Land Model, *J Adv Model
Earth Sy*, 4, doi:Artn M08002 10.1029/2012ms000165.

Williams, M., E. B. Rastetter, D. N. Fernandes, M. L. Goulden, S. C. Wofsy, G. R. Shaver, J. M.
580 Melillo, J. W. Munger, S. M. Fan, and K. J. Nadelhoffer (1996), Modelling the soil-plant-
atmosphere continuum in a *Quercus*-*Acer* stand at Harvard forest: The regulation of
stomatal conductance by light, nitrogen and soil/plant hydraulic properties, *Plant Cell
Environ*, 19(8), 911-927, doi:DOI 10.1111/j.1365-3040.1996.tb00456.x.

Xu, X. T., D. Medvigy, J. S. Powers, J. M. Becknell, and K. Y. Guan (2016), Diversity in plant
585 hydraulic traits explains seasonal and inter-annual variations of vegetation dynamics in
seasonally dry tropical forests, *New Phytol*, 212(1), 80-95, doi:10.1111/nph.14009.

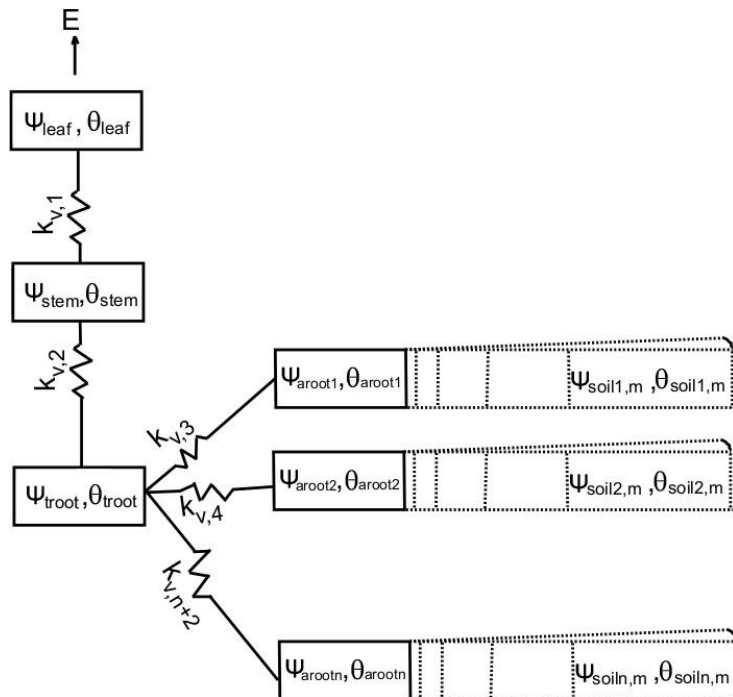
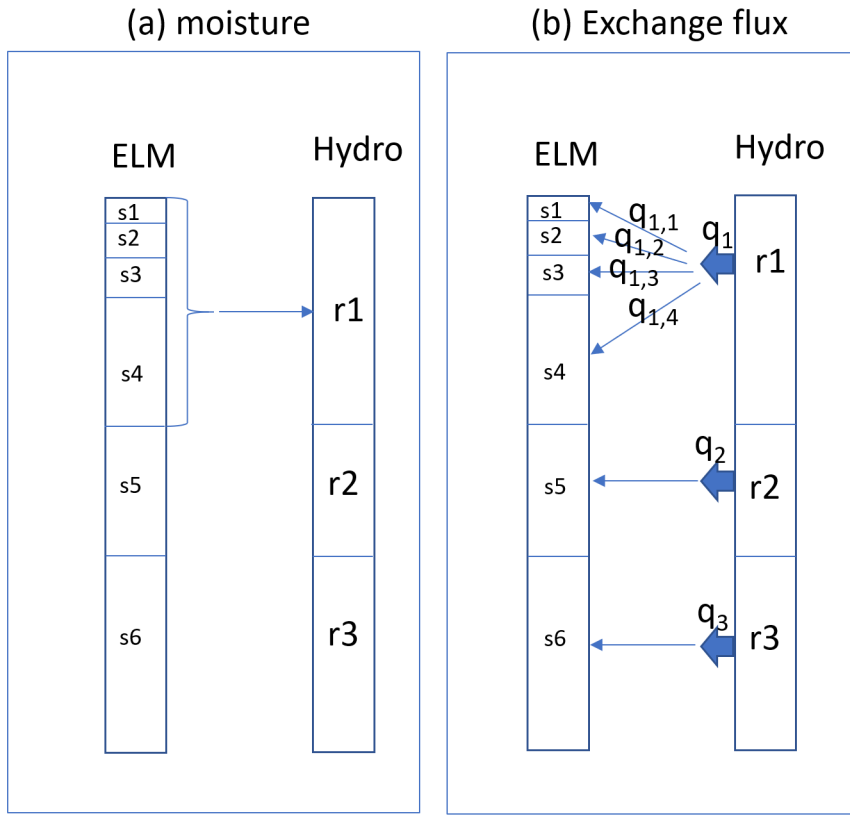
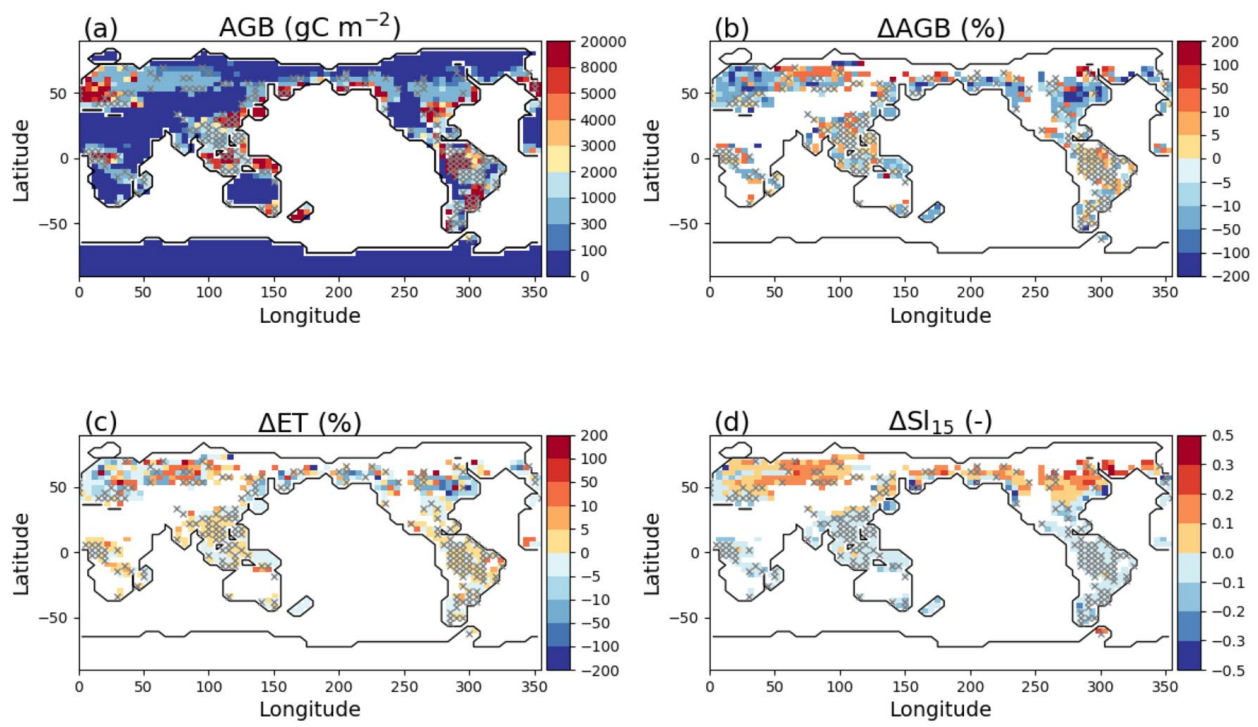


Figure 1. Schematic of FATES-hydro, with each box representing a compartment of plant tissue
or soil rhizosphere.





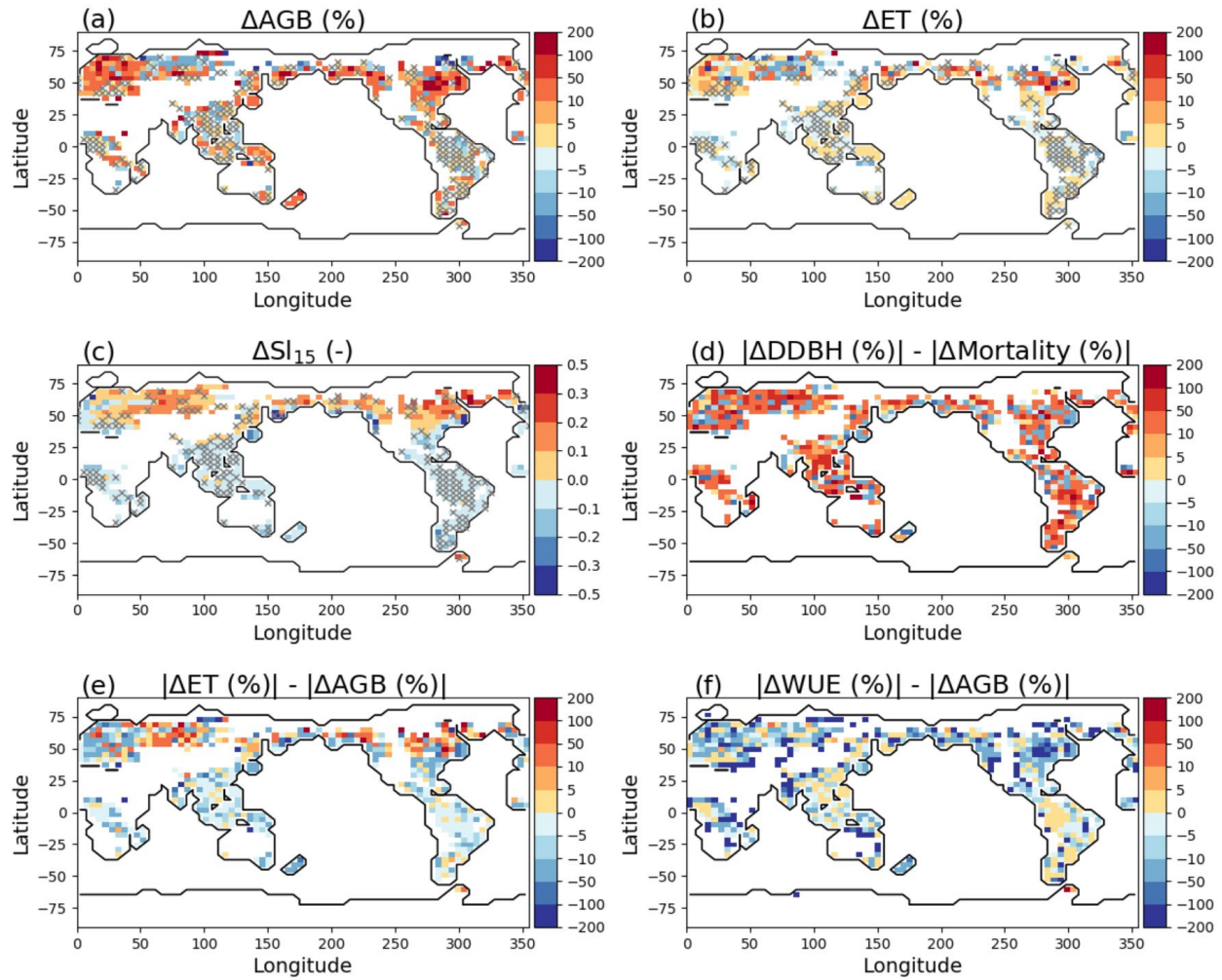
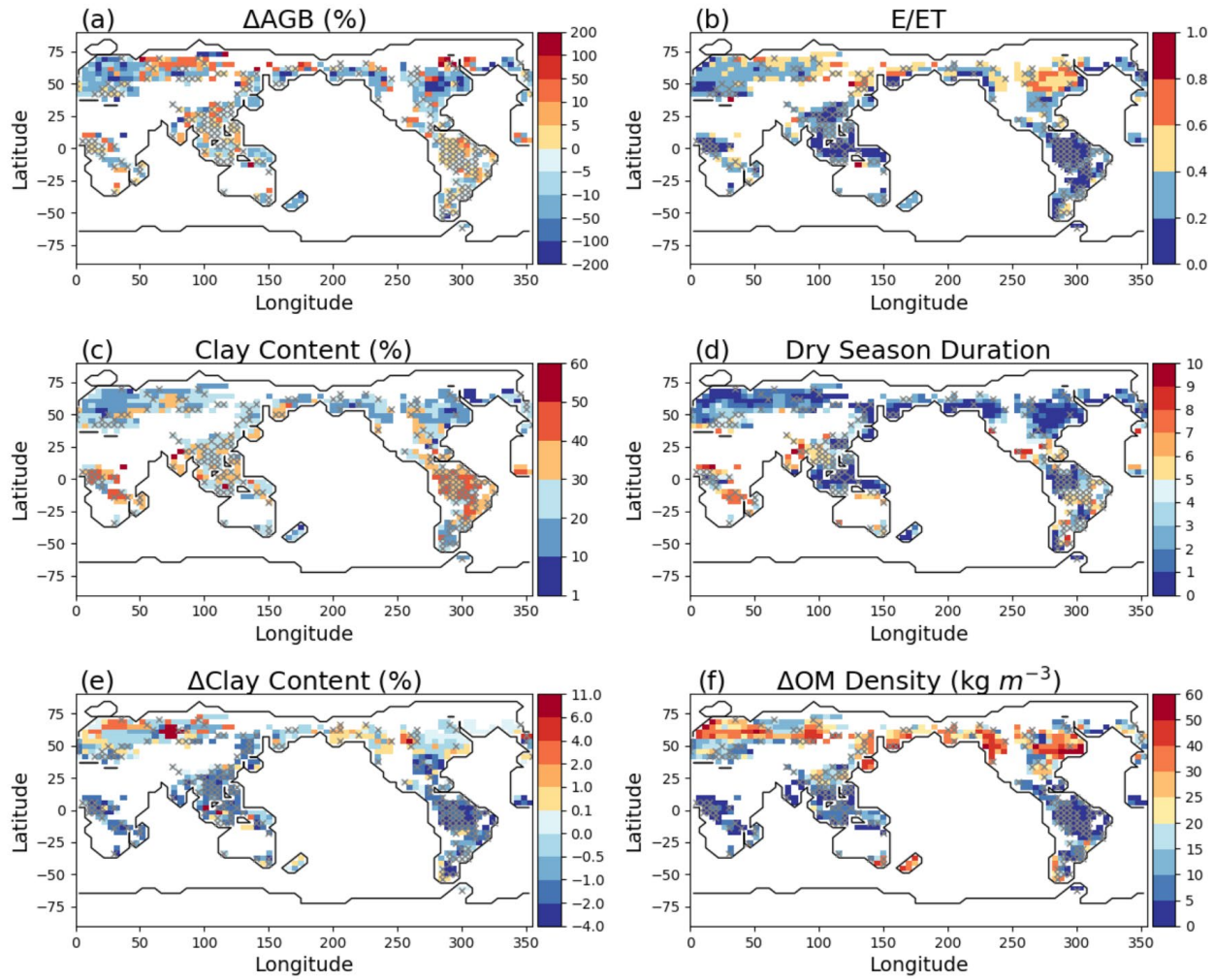
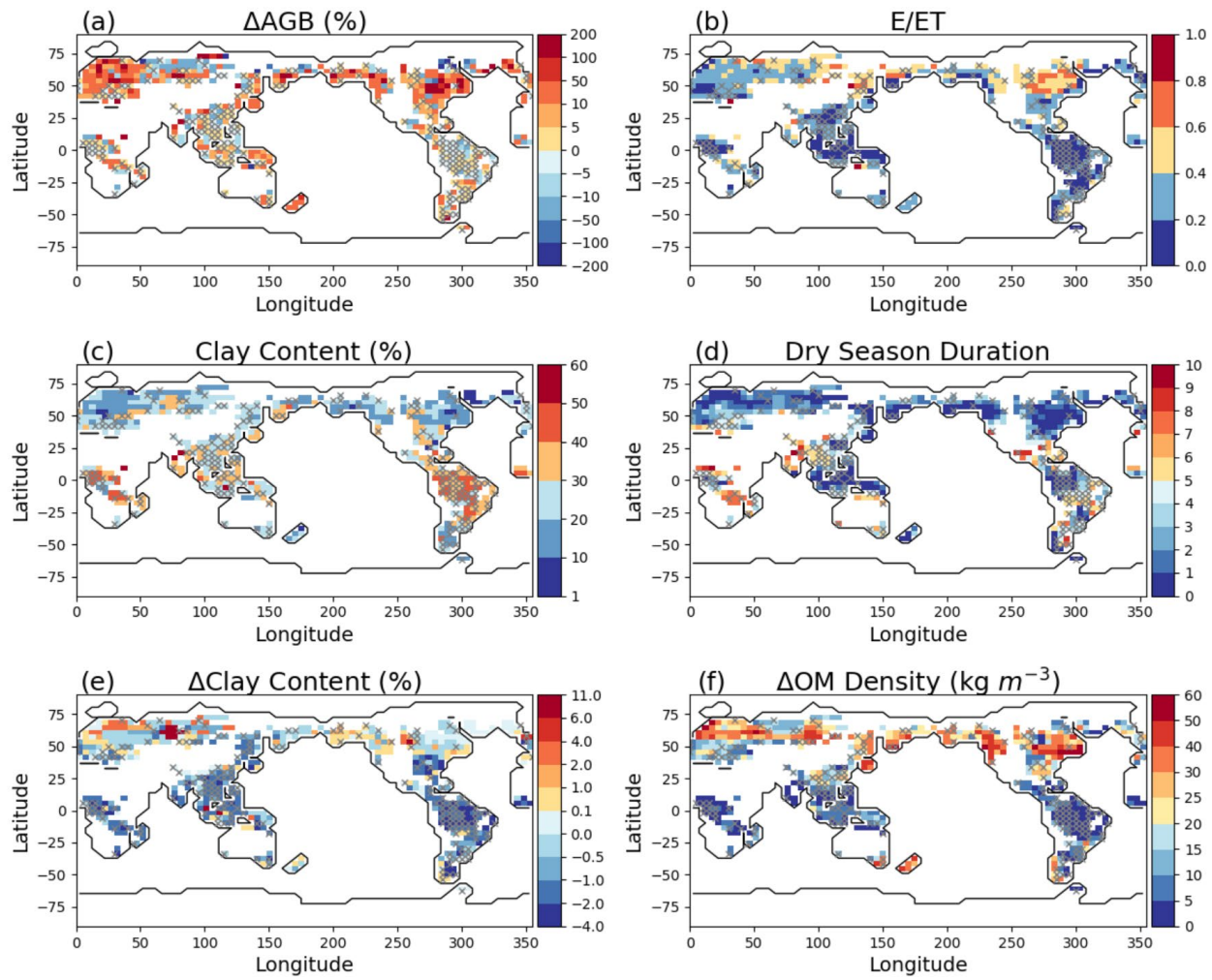
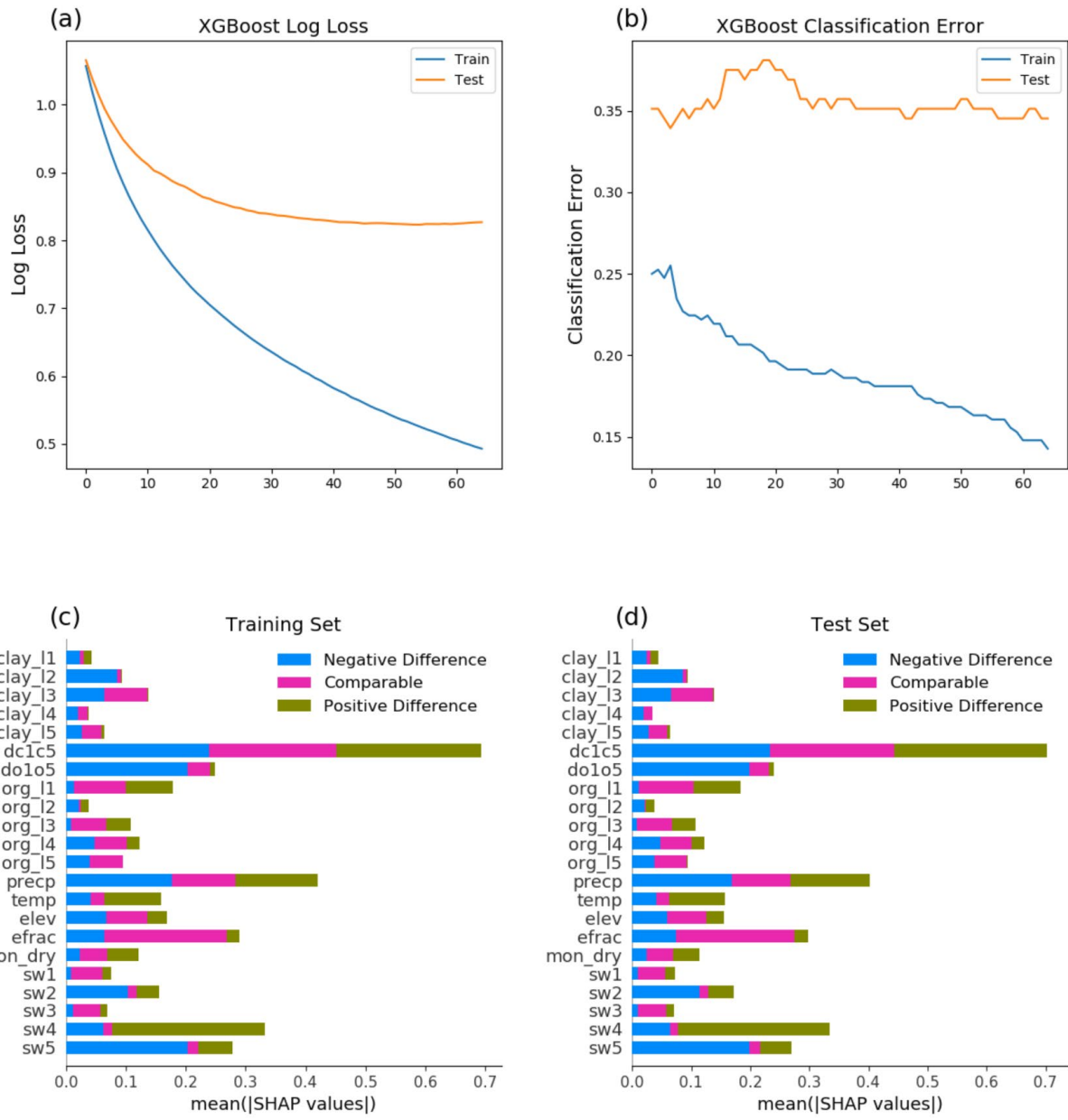


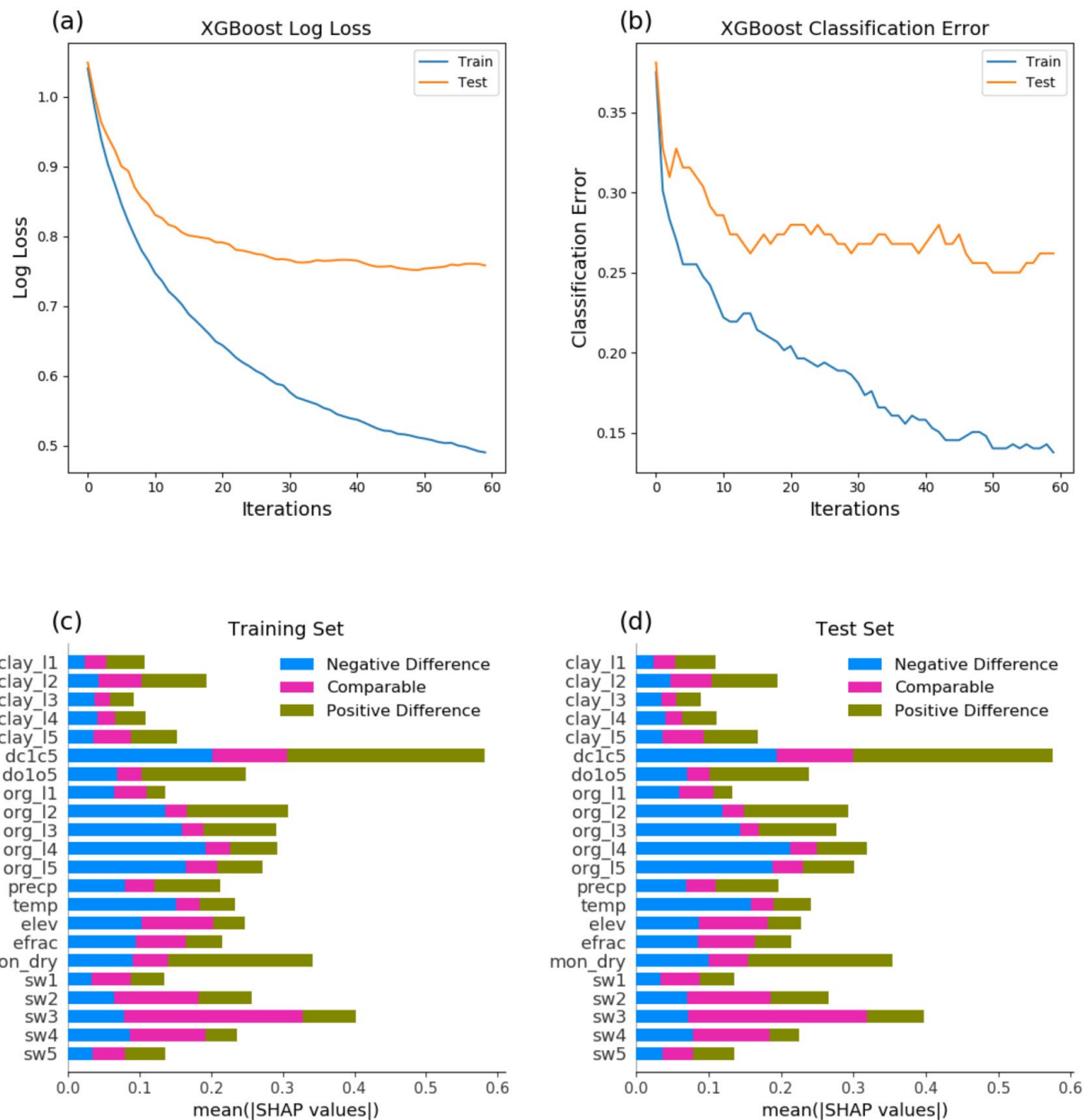
Figure 3. Average AGB in simulation year 100 (a), model difference resulted from layer aggregations: percent change of AGB (b) and percent change of ET (e), and (b), average soil water saturation between soil layer 1 and layer 5 in simulation year 100 (d) without layer aggregation, (c) for the Reference simulation, relative change of growth compared to the relative change of mortality (d), relative change of ET compared to the relative change of AGB (e), and relative change of WUE compared to the relative change of AGB (f). The pixels in white on land in (b,c,d) have values beyond the limits of the legends, associated with $AGB < 0.5 \text{ gC m}^{-2}$. Pixels with symbol \times have ΔAGB less than 5%.





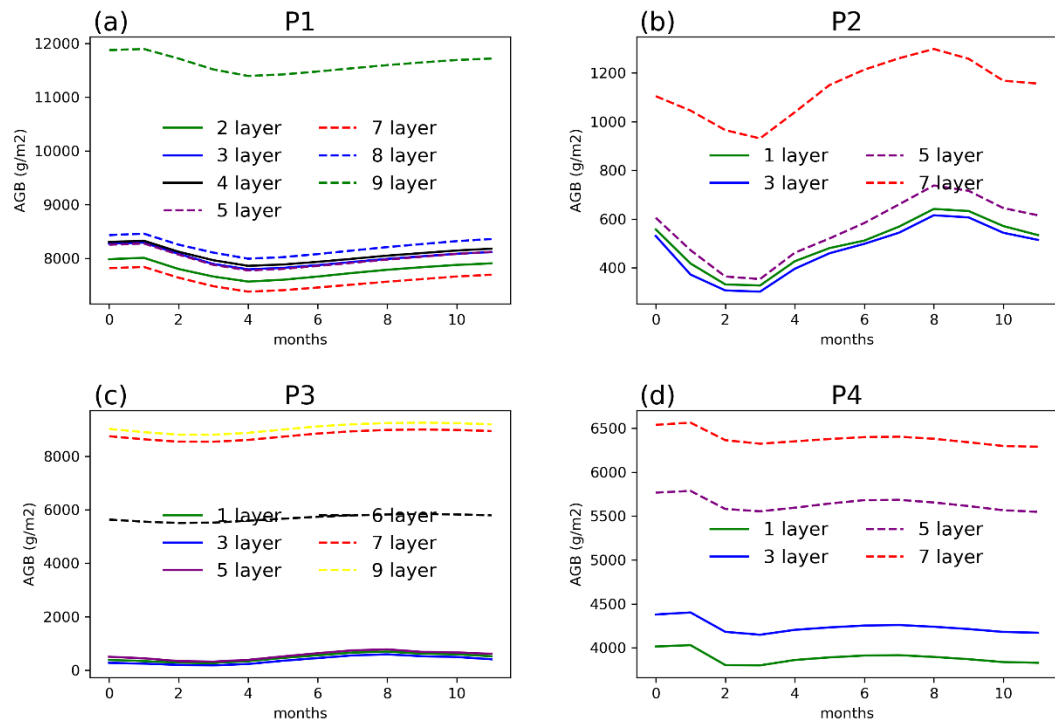
610 **Figure 4.** Model differences resulted from layer aggregations: percent change of AGB ~~between no layer aggregation and aggregating 5 layers (Experiment – Reference)~~ (a), and E/ET (b) for
 615 simulation year 100, average clay content in the soil column (c), and dry season durations (months) (d), clay content difference (e) and organic matter difference (f) between layer 1 and the average of the top 5 layers from the surface. The pixels in white on land have values beyond the limits of the legends, associated with $\text{AGB} < 0.5 \text{ gC m}^{-2}$. Pixels with symbol \times have AGB differences less than 5%.





620

Figure 5. XGBoost model evaluation using selected conditions as predictors: learning curve, logarithmic loss (a), learning curve, classification error (b), feature importance for the training set (c), and feature importance for the test set (d)



625

Figure 6. AGB from single point simulations at selected locations (P1 – P4) at year 100 of the simulations.

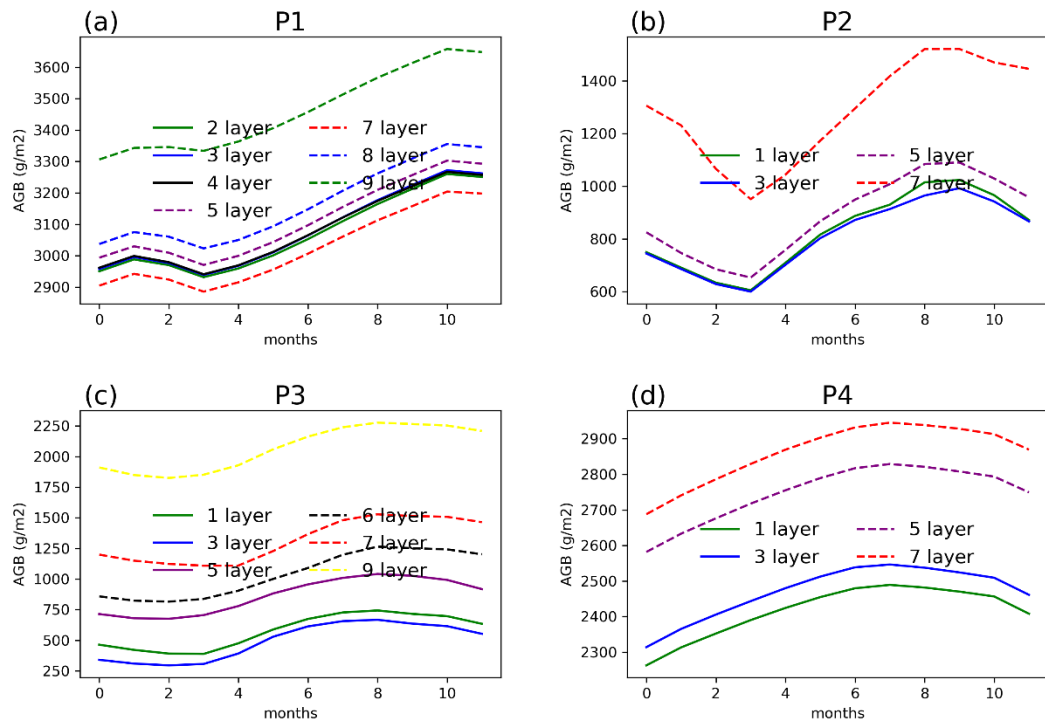
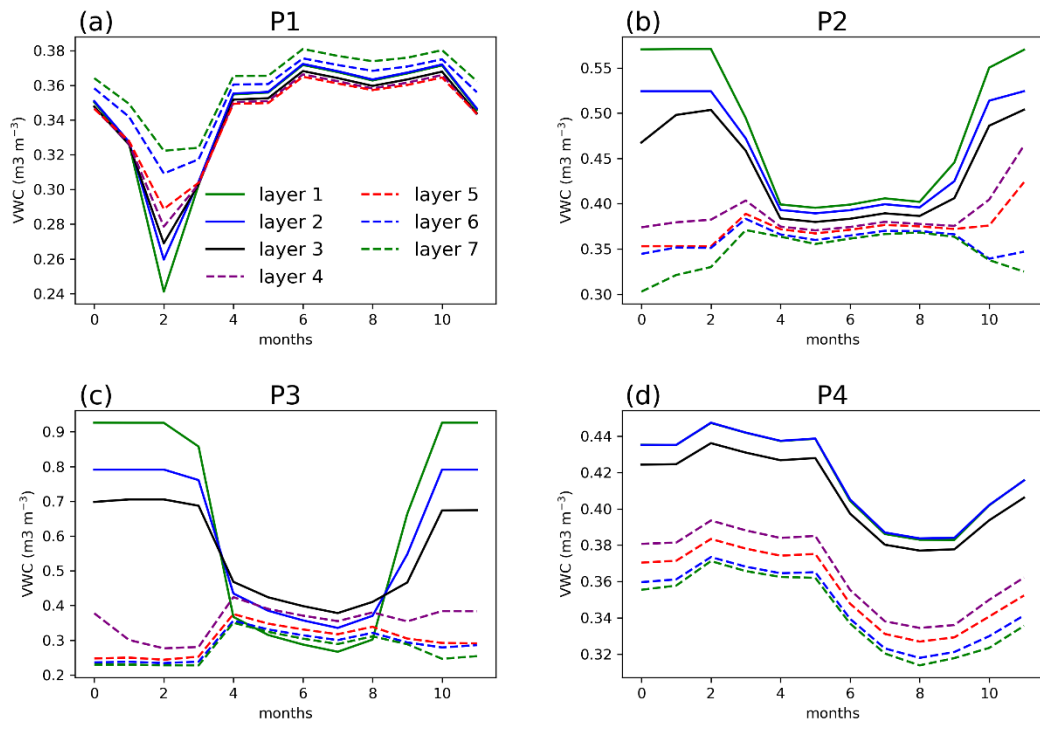
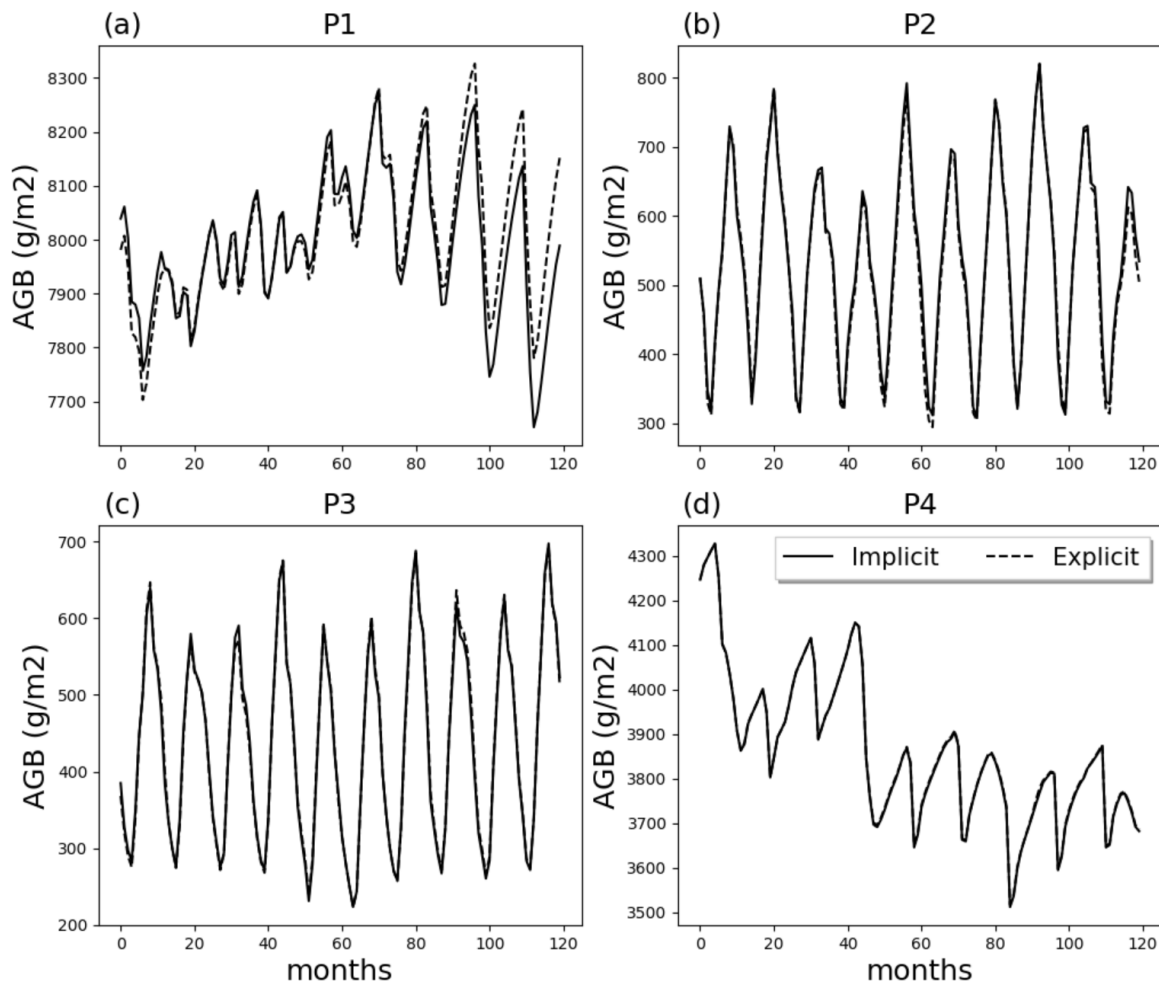


Figure 7. AGB from single point simulations at each selected location (P1 – P4) at year 10 of the simulations.



630

Figure 8. Volumetric water content (VWC) at selected points for single point simulations at 100 year of the simulation with no layer aggregation



635 **Figure 9.** Comparison of AGB in the last 10 simulation years at points P1 to P4 with implicit
and explicit integration methods.